Angewandte Chemie

Angewandte Chemie GDCh German Chemical Society

Zitierweise: *Angew. Chem. Int. Ed.* **2026**, 65, e4883376
doi.org/10.1002/anie.4883376

FORSCHUNGSARTIKEL

Dihydrogen Bond Cooperativity Resolves Zero-Linear Compressibility in an Energetic Crystal

Ye Cao[1] | Tianyu Jiang[2] | Lanxuan Sun[2] | Qingchao Zeng[3] | Feng Wang[1] | Shiliang Huang[2] | Kuo Li[3] | Guanjun Xiao[1] | Guangyu Qi[2] | Bo Zou[1]

[1]State Key Laboratory of High Pressure and Superhard Materials, College of Physics, Jilin University, Changchun, China | [2]Institute of Chemical Materials, China Academy of Engineering Physics (CAEP), Mianyang, China | [3]Center For High Pressure Science and Technology Advanced Research (HPSTAR), Beijing, China

Correspondence: Guanjun Xiao (xguanjun@jlu.edu.cn) | Guangyu Qi (qiguangyu@caep.cn)

Received: 21 January 2026 | **Revised:** 21 January 2026 | **Accepted:** 24 February 2026

Keywords: dihydrogen bonds | energetic material | high pressure | zero-linear compressibility

ABSTRACT

Zero linear compressibility (ZLC) energetic materials can be used as anti-shock materials to maintain stability in at high-pressure environments up to tens of gigapascals under shock conditions. Achieving an energetic material with ZLC properties and clarifying its structure–activity relationship should meet the urgent safety demands. In this study, the first ZLC organic molecular crystal, trimethylamine borane (TMAB), which can be utilized as a propellant component, was discovered. TMAB underwent an isostructural phase transition at 9.2 GPa, as evidenced by the combination of Raman, infrared, and UV–vis absorption spectra and in situ synchrotron x-ray diffraction patterns. Note that the *c* axis exhibited intriguing ZLC in the pressure range from 9.2 to 14.0 GPa, indicating the superior stability of TMAB under extreme high pressure. The dihydrogen-bonding cooperativity effect under high pressure was responsible for the observed ZLC in TMAB, unlike that observed for previously reported ZLC materials. This study developed a ZLC energetic organic molecular crystal and revealed its underlying mechanism, which facilitates the design of anti-shock propellants.

1 | Introduction

The fundamental thermodynamic principle states that materials generally shrink in all directions under the loading of hydrostatic pressure, that is, materials naturally exhibit positive linear compressibility (PLC) [1, 2]. Nevertheless, some substances even expand in one or two directions within a certain pressure range, known as negative linear or area compressibility (NLC/NAC) [3–10]. More rarely, very few materials neither contract nor expand along a specific direction but exhibit zero linear compressibility (ZLC) [11]. Such materials, which maintain the length in a certain direction upon compression, can be applied in unique systems, such as anti-pressure and anti-shock materials, precise instruments, and telecommunication optical fibers in the deep sea [12]. Organic molecular crystals exhibiting NLC have been in porous organic salts [13], energetic materials [14], and organic minerals [15], after the first report on NLC observation in methanol monohydrate by Fortes et al. (2011) [16]. However, only fewer than a dozen single-component ZLC materials have been discovered to date. ZLC materials can be divided into two types, as shown in Figure 1a, including superhard materials (e. g., diamond and elemental Os) [17–20] and materials with a specific structural configuration (e. g., MIL-122(In) [11] and $[C(NH_2)_3][Cd(HCOO)_3]$ [21] with a wine-rack structure, SrB_2O_4 and CaB_2O_4 with a Lu–Ban stool structure [22], $LiBO_2$ with a corrugated-graphite structure [23], $RbBe_2BO_3F_2$, and $CsBe_2BO_3F_2$ with a Lifshitz structure [24], $Li_2Ti(IO_3)_6$ with a gear-spring structure [25] and Cu_2GeO_4 with a microscopic orthogonal-braiding structure [26]).

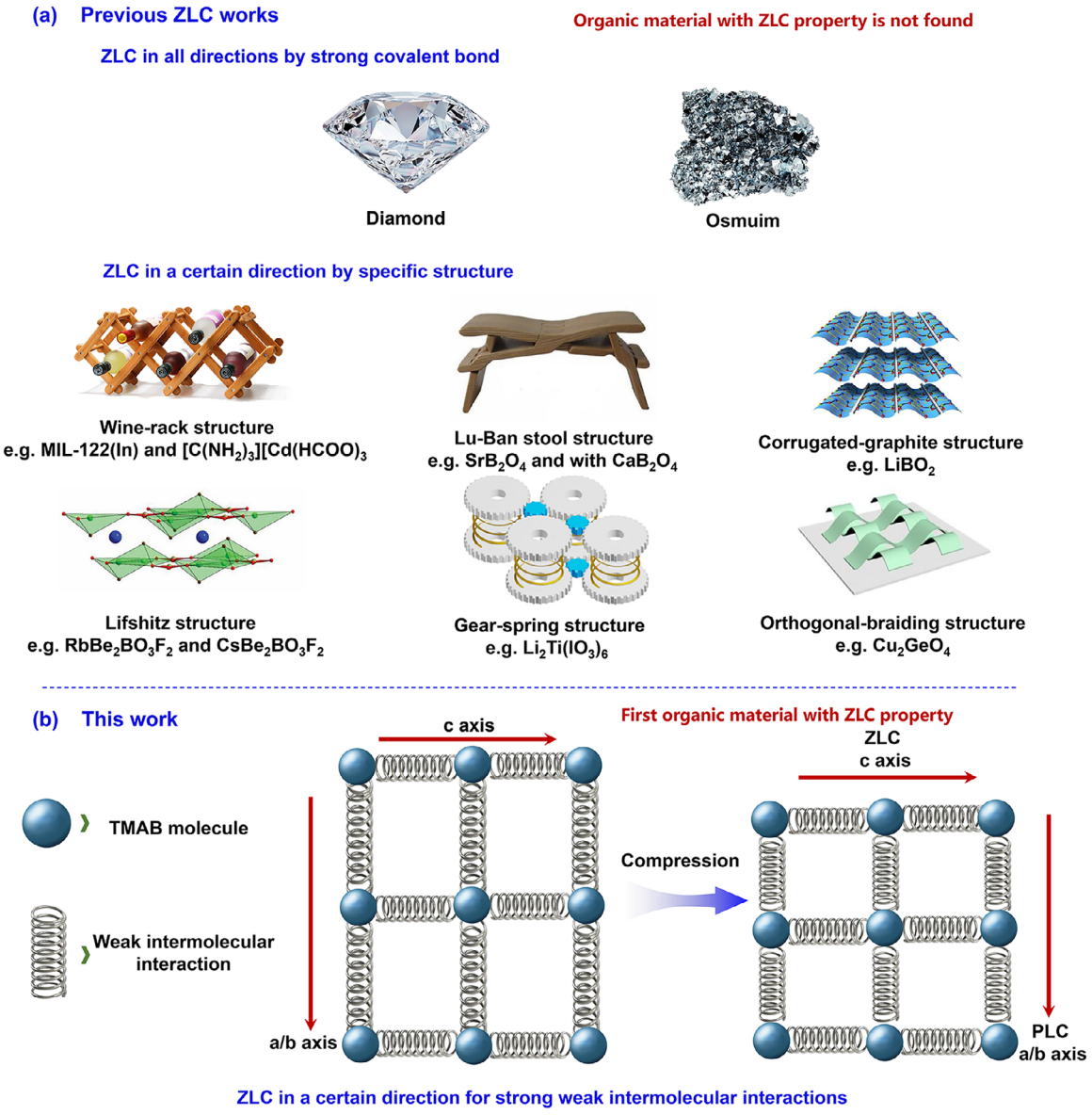

FIGURE 1 | (a) Previous ZLC works of inorganic compounds. (b) This ZLC work by weak intermolecular in TMAB.

Diamond and osmuim resist compression in all directions owing to their strong covalent bonds. Compounds with specific structures can maintain ZLC in a certain direction but display normal PLC in other directions. The strength and formation of covalent bonds in specific structures play key roles in the development of ZLC materials. However, the ZLC behavior of organic crystals dominated by weak interactions has not yet been elucidated. Finding a ZLC organic material constructed by weak interactions and establishing its structure–property relationship will promote the fabrication of materials with abnormal compressibility and provide a strategy to design new functional ZLC materials.

Energetic materials are a class of specialized functional materials that rapidly release large amounts of energy under certain stimuli [27–30]. Energetic materials, including explosives, pyrotechnics, and propellants, have widespread applications in mining, blasting, petroleum drilling, space exploration, and the military [31–36]. As the energy source of missiles and rockets, propellants are possibly exposed to an environment of up to tens of gigapascals under shock conditions [37]. Therefore, large-scale compressibility, phase transitions, and even direct decomposition occur, resulting in the structural destruction of devices [38, 39]. In this regard, developing an energetic material with ZLC properties and clarifying its structure–activity relationship will greatly meet the urgent safety demands of weapons and launch vehicles. Nonetheless, energetic materials with ZLC property remain elusive.

Here, we firstly discovered a ZLC energetic organic molecular crystal, trimethylamine borane (TMAB), which crystallizes via weak intermolecular interactions (Figure 1b) and could be utilized as a propellant component because of its high hydrogen content (16.45% by weight) [40, 41]. The ZLC behavior of TMAB was investigated using in situ high-pressure angle-dispersive x-ray diffraction (ADXRD), Raman spectra, infrared (IR) spectra, UV–vis absorption spectra, and first-principles calculations. TMAB did not undergo a structural phase transition, but experienced an isostructural phase transition upon compression

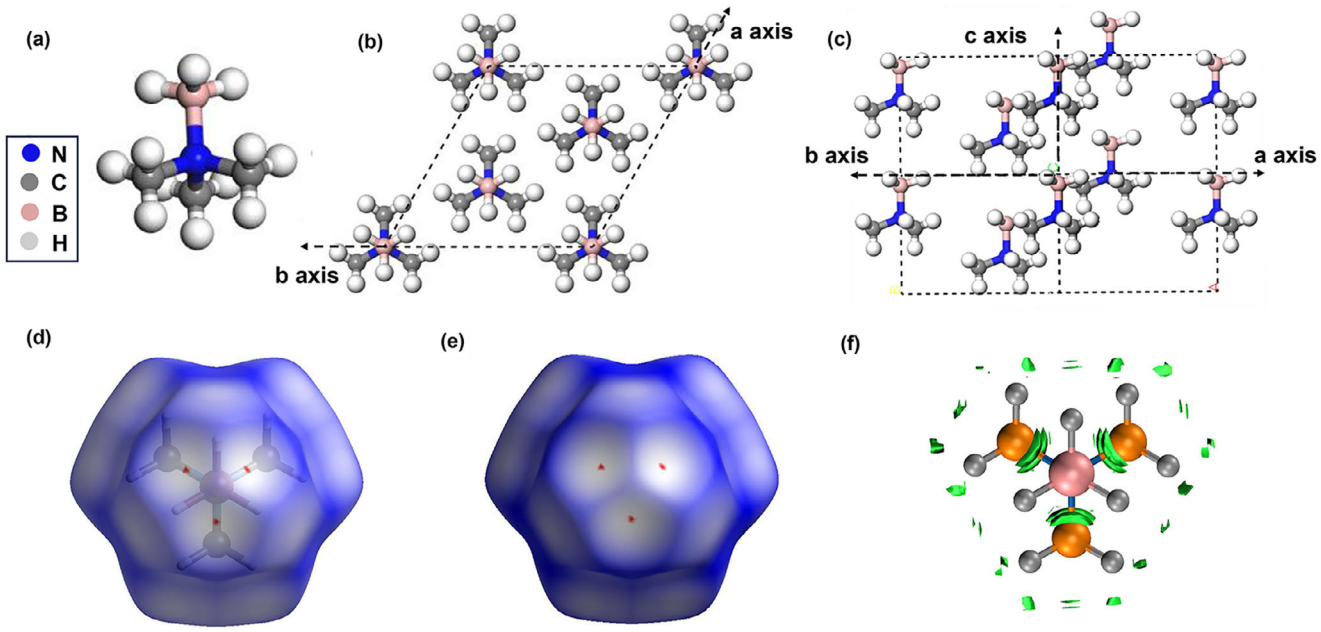

FIGURE 2 | (a) Molecular structure of TMAB. (b and c) Molecular packing in different directions. (d) Transparent Hirshfeld surface of TMAB. (e) Hirshfeld surface of TMAB. (f) IMGH isosurface of TMAB at ambient pressure with isovalue = 0.007. The green represented for van der Waals' forces.

at approximately 20 GPa (close to the detonation pressure of TNT), highlighting its excellent high-pressure structural stability. Furthermore, the *c* axis exhibited intriguing ZLC in the pressure range from 9.2 to 14.0 GPa, indicating the superior stability of TMAB against extremely high pressure. Different from the inorganic crystals or metal-organic frameworks with ZLC properties, TMAB only exhibited a simple structure, which is different from that of other ZLC materials. The dihydrogen bonding cooperativity effect under high pressure was highly responsible for the observed ZLC in TMAB. Basic guidelines for the structural design of ZLC molecular crystals with the bonding cooperativity effect were reasonably proposed. Our findings establish a fundamental relationship between the structural evolution and weak intermolecular interactions of TMAB, and highlight the potential of a ZLC energetic organic molecular crystal as a promising component in hydrogen-rich propellants.

2 | Results and Discussion

TMAB crystallized in the space group of *R3m* with lattice parameters $a = b = 9.1065(14)$ Å, $c = 5.9068(10)$ Å under ambient conditions. The molecular and crystal structures of TMAB exhibit high symmetry, as depicted in Figure 2a–c, respectively. Both the BH_3 group and three CH_3 groups are distributed equally along the B—N bond, therefore, the TMAB molecule has a three-fold rotational symmetry. The TMAB molecules are connected via normal van der Waals' forces in the *a*/*b* axis over a long distance between molecules. Along the *c* axis, the ternary weak C—H···H—B intermolecular interactions link the adjacent molecules to generate a one-dimensional TMAB tape, as displayed in Figure 2c. We further performed Hirshfeld surface analysis to analyze the weak ternary intermolecular interactions, as shown in Figure2d,e. The color changed from blue to white and finally to red, indicating the gradual increase in the intensity of the weak intermolecular interactions. Only three small red points are present in the Hirshfeld surface, illustrating that the intensity of C—H···H—B interactions is comparatively weak [42]. The IMGH isosurface was also used to ascertain the type of these weak interactions and confirmed that the C—H···H—B interactions at ambient pressure are characterized as van der Waals' forces (Figure 2f). As the H atom almost covered the B, C, and N atoms, the fingerprint plots were all attributed to H···H interactions (Figure S1). The plots nearer to the origin are representative of relatively strong C—H···H—B interactions, and the plots farther from the origin are representative of relatively weak van der Waals' forces. These plots are farther from the origin compared with those of other B—N—H compounds, which also manifested the low intensity of the C—H···H—B interactions. Owing to its high hydrogen capacity, TMAB can be used as a component of propellants, which may face high-pressures under shock conditions. The most widely used explosive, TNT, can produce a high-pressure of approximately 20 GPa. Therefore, the propellants in missiles or rockets may experience pressures up to 20 GPa under the attack of TNT-filled weapons. We performed in situ synchrotron ADXRD measurements of TMAB up to 20 GPa to directly provide information about the pressure-induced structural variations, as shown in Figure 3a. All XRD patterns obtained in our experiment and the original XRD images are depicted in Figures S2–S8, respectively. The diffraction peaks evolved continuously upon compression and no other peaks were generated during compression to 20.1 GPa. The intensities of the peaks decreased gradually, indicating that the crystallinity decreased. After pressure quenching, the intensity and location of diffraction patterns were recovered (Figure S9), manifesting that the high-pressure structural variation of TMAB was reversible. High-pressure single-crystal XRD was also performed at 0.7 and 19.0 GPa, the patterns shown in Figures S10 and S11 provide more information about the pressure-induced structural evolvement. We did not observe any other diffraction patterns that did not belong to the initial space group of *R3m*, indicating that TMAB did not undergo a structural phase transition. To obtain

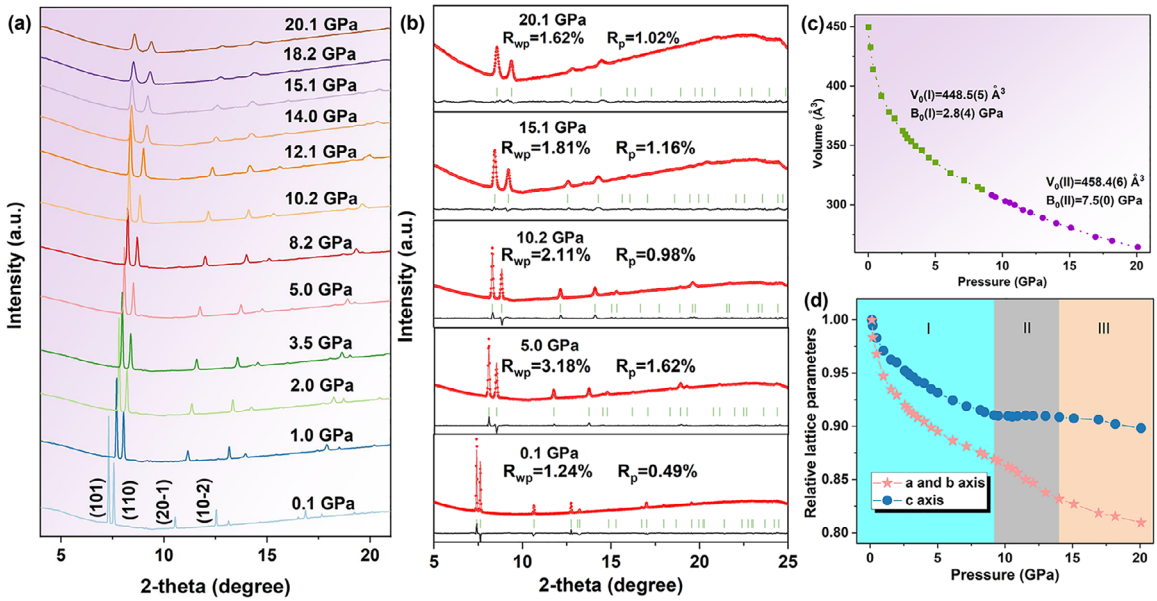

FIGURE 3 | (a) In situ high-pressure synchrotron ADXRD spectra of TMAB. (b) Rietveld refinement of ADXRD patterns. (c) Pressure–volume relationship fitted by third order Birch–Murnaghan equation of state. (d) Relative lattice parameters at pressures.

the accurate lattice parameters of TMAB at different pressures, Rietveld refinement was performed, as in other well-established reports. [43–45] Selected refinements of the ADXRD patterns are depicted in Figure 2b, the low values of R_{wp} and R_p illustrate that the lattice parameters obtained from the experimental data were convincing. Peak shifts of XRD patterns were recorded. The (110) peak determined by the *a/b* axis shifted faster than other patterns above 9.2 GPa indicating that the *c* axis exhibited a lower compression rate than the *a/b* axis (Figure S12).

The volumes of TMAB at different pressures were achieved by the refinement and a discontinuity was observed at 9.2 GPa, indicating that an isostructural phase transition may occur at this pressure. To further analyze the structural evolution, the experimental pressure–volume data were fitted (Figure 3c) in two pressure ranges from 0.1 to 9.2 GPa and from 9.2 to 20.1 GPa via the third order Birch–Murnaghan equation of state. The equation is as follows:

$$P(V) = \frac{3B_0}{2}\left[\left(\frac{V_0}{V}\right)^{\frac{7}{3}} - \left(\frac{V_0}{V}\right)^{\frac{5}{3}}\right]\left\{1 + \frac{3}{4}\left(B_0' - 4\right)\left[\left(\frac{V_0}{V}\right)^{\frac{2}{3}} - 1\right]\right\}$$

where V_0 is the zero-pressure volume, B_0 is the bulk modulus at ambient pressure, and B_0' is a parameter for the pressure derivative. The B_0' is fitted with an original value of 4. The bulk modulus (B_0) was 2.8(4) GPa and 7.5(0) GPa before and after 9.2 GPa. Judging from the low value of B_0, TMAB can be readily compressed. This can be explained by the low intensity of intermolecular interactions. The compression is highly anisotropic with the *a/b* axis direction being more compressible than the *c* axis direction during the entire compression process. The *c* axis underwent three notable regions with different compressibilities from ambient pressure to 20.1 GPa. In region I from ambient pressure to 9.2 GPa, the *c* axis was significantly compressed. While it exhibited a high stability in region II from 9.2 to 14.0 GPa, and finally shrank moderately from 14.0 to 20.1 GPa.

Goodwin et al. developed an online PASCal program [46], which has been widely utilized to analyze compressibility and thermal expansion [13, 45, 47]. For systems of orthorhombic symmetry or higher, the principal and (conventional) crystallographic axes coincide, the variation in lattice parameters ℓ with pressure (P) is related directly to compressibilities $K\ell$.

$$K\ell = -\frac{1}{\ell}\left(\frac{\partial \ell}{\partial P}\right)$$

To get the exact compressibility of each axis in the three pressure ranges, we calculated the linear compressibility of the unit cell using the PASCal program, as depicted in Figure 4a–f and Table S1. The *c* axis has the same direction as the X_3 axis, and the plane constructed by *a* and *b* axis is the same as the X_1–X_2 plane. The *a/b* axis can create an angle of any degree with the X_1 or X_2 axis (Figure S13). Within the pressure range from the ambient pressure to 9.2 GPa, the X_1/X_2 axis rarely presented a larger PLC value (11.8663 TPa^{-1}) than that (9.0715 TPa^{-1}) of the X_3 axis (*c* axis), indicating that *a/b* axis has a larger compressibility. In addition, the value of K_{X1}, K_{X2}, and K_{X3} decreased sharply at pressures, indicating that compressibility was significantly reduced during the initial pressure loading process. The compressibility indicator is presented as a red ellipsoid, with X_1/X_2 as the long axis and X_3 (*c*) as the short axis (Figure 4b). In the pressure range from 9.2 to 14.0 GPa, X_1/X_2 also exhibited a PLC value of 9.4356 TPa^{-1}. Note that the *c* axis or X_3 axis rarely presented a very low linear compressibility value of 0.155 TPa^{-1}. Based on the definition, the linear compressibility value shows that the X_3 axis (*c* axis) of TMAB exhibits typical ZLC behavior, which is also the first ZLC phenomenon in organic molecular crystal structure. The compressibility indicator showed a doughnut shape for the zero compressibility value on *c* axis. Upon further compression to 20.1 GPa, both the X_1/X_2 and X_3 axes recovered to PLC (Figure 4e, f)

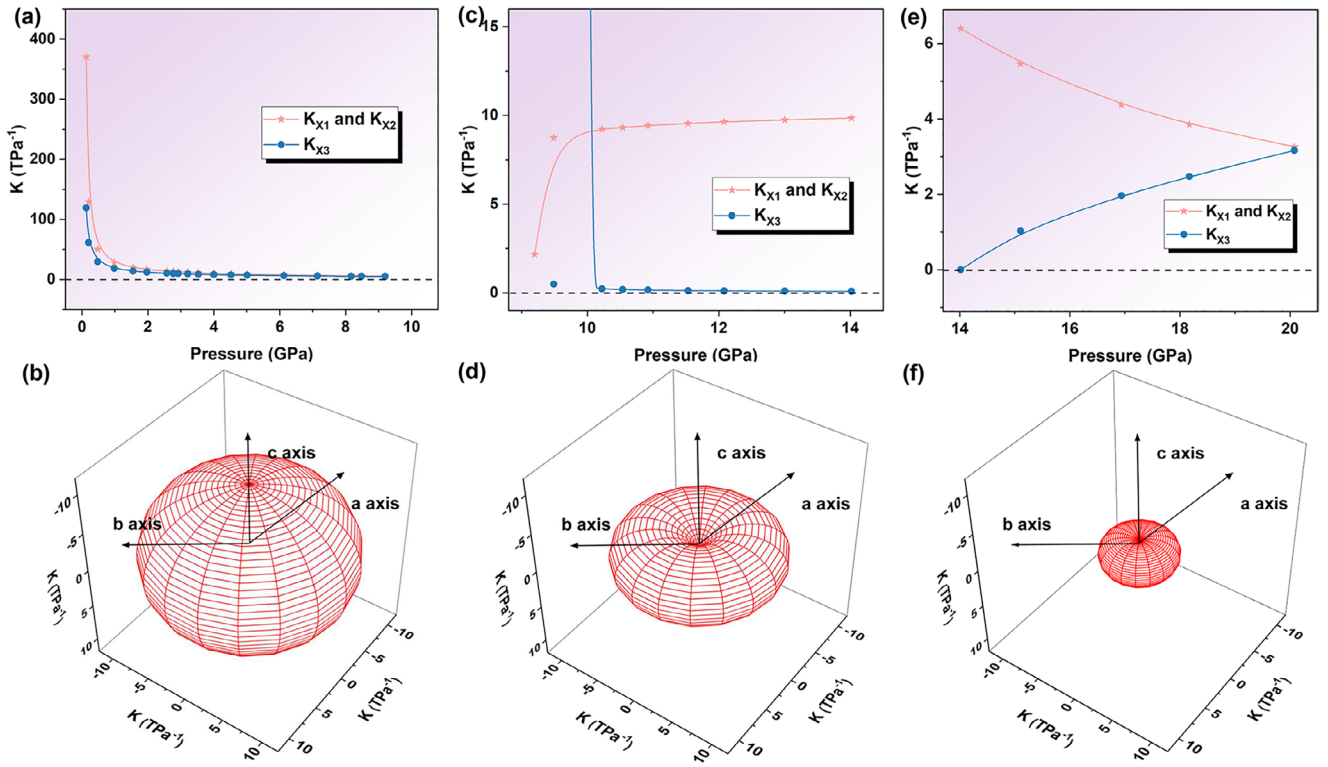

FIGURE 4 | (a) Linear compressibility of the unit cell from the ambient pressure to 9.2 GPa calculated by online program PASCal. (b) Compressibility indicatrix of TMAB from the ambient pressure to 9.2 GPa. (c) Linear compressibility of the unit cell from 9.2 to 14.0 GPa. (d) Compressibility indicatrix from 9.2 to 14.0 GPa. (e) Linear compressibility of the unit cell from 14.0 to 20.1 GPa. (f) Compressibility indicatrix from 14.0 to 20.1 GPa. The red portion represents PLC effect.

with small compression values of 4.3749 and 1.9682 TPa^{-1} (lower than the initial compression values of the X_1/X_2 and X_3 axes), respectively. Therefore, the compressibility indicator exhibits a smaller tabular red ellipsoid.

In situ high-pressure Raman, IR, UV–vis absorption spectra and first-principles calculation were carried out to obtain more information on this abnormal high-pressure structural evolution in TMAB, Raman and IR spectra can reflect the vibrational modes of chemical bonds, thus indirectly giving more information on the structural evolvement of TMAB at different pressures. The Raman and IR modes were assigned according to previous studies in Table S2 [42]. In the Raman spectra, the patterns evolved continuously before 9.9 GPa, while some abrupt changes were generated upon further compression to 9.9 GPa (Figure S14). Three new modes assigned to BH_3 deformation, formed at 1018, 1089, and 1232 cm^{-1} (marked with an up-ward arrow), and the CN stretching mode at 970 cm^{-1} (marked with a down-ward arrow) vanished gradually. In the CH_3 distortion modes region, a mode was generated at 1425 cm^{-1} and the peak at 1510 cm^{-1} reduced in intensity. Both BH and CH stretching modes also exhibited some remarkable changes, for instance the occurrence of new BH and CH stretching modes at 2460 and 3096 cm^{-1}. In addition, the Raman shifts of TMAB evolved discontinuously at 9.9 GPa (Figure S15). Moreover, in the IR spectra, a new CH_3 distortion mode (marked with an upward arrow in Figure S16) was generated at 1474 cm^{-1}. After the pressure was released, the Raman and IR spectra were recovered as ADXRD measurement (Figures S17 and S18). Based on the ADXRD, Raman, and IR spectroscopy results, an isostructural phase transition was confirmed [48–50]. As isostructural phase transitions often occur with variations in the electronic structure, further UV–vis absorption spectra were performed to help understand the electron structural variation of TMAB at different pressures as shown in Figure S19. The absorption peak at approximately 238 nm disappeared at 10.1 GPa, indicating the structural changes in electrons. Generally, once a structural phase transition happened, single crystal breaks because of molecular twisting or rearrangement. The optical photographs in Figure S20 indicate that the TMAB crystal was transparent during the entire compression process, and no cracks were observed, indicating that this transformation was associated with an isostructural phase transition. The isostructural phase discovered was in accordance with that described in the previous report, which also suggested an impalpable phase transition of TMAB at 9.15 GPa [48].

Notably, BH stretching modes in the range from 2250 to 2600 cm^{-1} and CH stretching modes in the range from 2800 to 3230 cm^{-1} in Raman spectra shifted faster than the other vibration modes. We concluded that the covalent bonds related to CH···H-B interactions distinctly reduced their bond length and increased their intensity significantly under pressure. At 9.9 GPa, CH and BH related vibration modes exhibited significant changes, indicating that the C—H···H—B interactions would possibly convert from van der Waals forces to dihydrogen bonds. Raman and IR spectra gave the solid evidence that the covalent bonds were enhanced upon compression, accompanied by the strengthening of weak intermolecular interactions. Considering the high intensity of

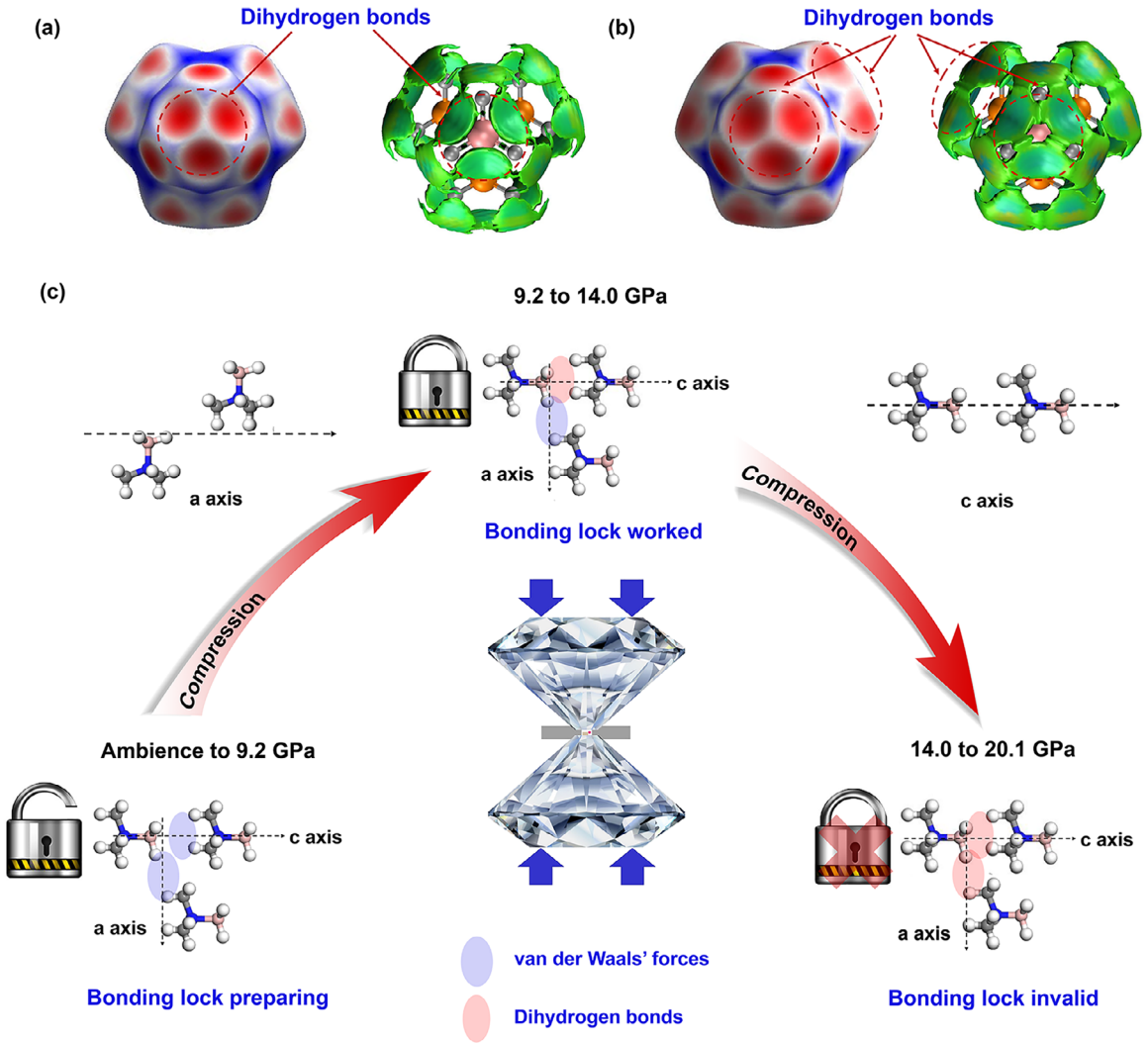

FIGURE 5 | (a) Hirshfeld surface and IMGH isosurface of TMAB at 10 GPa with isovalue = 0.007. (b) Hirshfeld surface and IMGH isosurface of TMAB at 20 GPa. The crystal structure was achieved through DFT calculations. The blue represented dihydrogen bonds in IMGH isosurface. (c) Weak intermolecular interaction in TMAB upon compression.

covalent bonds, which cannot be significantly influenced by weak intermolecular interactions, the compression behavior of TMAB was dominated by the synergistic effect of van der Waals' forces and the possibly newly generated dihydrogen bonds under high pressure. Therefore, we performed pressure-dependent Hirshfeld surface and IMGH analyses to elucidate the mechanism underlying the abnormal compressibility of TMAB. The small differences in lattice parameters between the structures achieved from first-principles calculations and those observed experimentally, as listed in Table S3, indicate that the weak intermolecular simulations were reliable. For the highly symmetric crystal structure of TMAB, the compressibility of X_1 and X_2 axes showed a positive correlation with that of the *a* and *b* axes, whereas the X_3 and *c* axes were in the same direction. Therefore, we can analyze the weak intermolecular interactions at various pressures along the crystal axis to understand ZLC behavior. As shown in Figure 2c, TMAB molecules are connected from head to tail via ternary C—H···H—B interactions along the *c* axis to generate a 1-D tape. The C—H···H—B interactions exhibit a small angle with the *a/b* axis, both of which are in almost the same direction. The TMAB molecules are located in a zigzag arrangement along the *a/b* axis.

The dominant weak interactions along the *a/b* and *c* axes were van der Waals' forces at ambient pressure. Based on the crystal structure simulated using VASP, we performed Hirshfeld surface and IMGH isosurface analyses to clarify the weak interactions along the *a/b* and *c* axes at 10 and 20 GPa (Figures 5a,b, S21 and S22), respectively. The proportion of red region on Hirshfeld surface distinctly increased at 10 GPa, in relation to those under ambient conditions, indicating the strengthened weak interactions. The IMGH isosurface of TMAB further manifested that the C—H···H—B interactions along the *c* axis changed from van der Waals' forces to dihydrogen bonds, as evidenced by the color change in isosurface (Figure 5a). In contrast, the C—H···H—B interactions along the *a/b* axis were retained as van der Waals' forces. When the pressure increased to 20 GPa, both the C—H···H—B interactions along the *a/b* and *c* axes changed to dihydrogen bonds (Figure 5b). Therefore, the ZLC of *c* axis in TMAB was attributed to the pressure-enhanced dihydrogen bonding cooperativity effect, and the dihydrogen bonding could be regarded as a lock, as depicted in Figure 5c. In the low-pressure region from ambient pressure to 9.2 GPa, both the *a/b* and *c* axes exhibited normal PLC. The compressibility rate reduced

and the bonding lock was prepared to freeze the compression of *c* axis. When compressed to approximately 10 GPa, the weak interactions along the *c* axis were enhanced to satisfy the intensity of dihydrogen bonds, and the weak interactions along the *a/b* axis were still van der Waals' forces. The bonding lock eventually resulted in the ZLC of *c* axis. Upon further compression, the weak interactions along *a/b* and *c* axes changed to dihydrogen bonds, which were difficult to compress. The bonding lock along the *c* axis was invalid, and all the axes of TMAB recovered to PLC. Considering the relationship between the structural characteristics and abnormal compressibility of TMAB, we suggest that ZLC in organic molecules by weak interactions should meet the following rules. First, a relatively stronger weak intermolecular interaction should be located in a certain direction, such as the pressure-enhanced dihydrogen bonds in the *c* axis of TMAB. Second, the weak intermolecular interactions along the other directions were not very strong, so the other axes would be readily compressed. Finally, the weak interactions should be stable to keep the structure unchanged upon compression. In the present TMAB, the ternary dihydrogen bonds formed an extremely stable shape, thereby avoiding the rearrangement of weak interactions during the pressure-enhanced process.

Repeated in situ Raman spectroscopy was performed to determine structural reversibility, as depicted in Figure S23. The Raman bands recovered their original positions even after five compression cycles at 20 GPa, indicating the reversibility of the high-pressure variation of TMAB. Although, the intensity of Raman spectral bands decreased with increasing compression time, no other Raman patterns belonging to the decomposition products of TMAB were observed. The decreased intensity of Raman bands was caused by the poor crystallinity due to compression, not by the decomposition of TMAB. During the first compression to 20 GPa, the quenched sample maintained 80% of the original Raman bands intensity. The propellant material, TMAB, exhibited excellent stability, did not undergo an apparent structural phase transition, and even displayed ZLC behavior in the pressure range from 9.2 to 14.0 GPa, indicating that TMAB can be utilized as an anti-shock energetic material.

3 | Conclusion

The compressibility of TMAB was systematically explored via in situ high-pressure ADXRD, high-pressure single crystal XRD, Raman, IR, UV–vis absorption spectroscopy and first-principles calculations. ZLC in organic molecular crystal constructed by weak interactions was firstly discovered experimentally. In contrast to that of the previously reported ZLC materials, the ZLC of TMAB did not result by strong covalent bonds or specific structures. By combining the Raman spectra, IR spectra, Hirshfeld surfaces and IMGH isosurfaces, we propose a new dihydrogen bonding cooperativity strategy that is responsible for the abnormal ZLC of *c* axis in TMAB. Three basic rules were put forward for the future design of molecular functional materials with ZLC property, according to the relationship between compressibility and the characteristics of weak intermolecular interactions in TMAB. Our research provides deep insights into the ZLC phenomenon observed in organic molecular crystals and reveals an anti-shock energetic material, which can be utilized as a component of hydrogen-rich propellants.

Acknowledgements

This work is supported by the National Natural Science Foundation of China (Nos. 22475198, 22205219, T2521005, 12174144 and 12474009), the China Academy of Engineering Physics (CAEP) Foundation (No. CX20240007) and Fundamental and Interdisciplinary Disciplines Breakthrough Plan of the Ministry of Education of China (JYB2025XDXM403). This work was performed at BL15U1 at the Shanghai Synchrotron Radiation Facility (SSRF). The authors would like to thank the stuffs from Shanghai Synchrotron Radiation Facility (SSRF) Beamline BL15U1 and User Experiment Assist System.

Conflicts of Interest

The authors declare no conflicts of interest.

Data Availability Statement

The data that supports the findings of this study are available in the Supporting Information of this article

References

1. H. K. Mao, X. J. Chen, Y. Ding, B. Li, and L. Wang, "Solids, Liquids, and Gases under High Pressure," *Review of Modern Physics* 90 (2018): 015007, https://doi.org/10.1103/RevModPhys.90.015007.

2. A. B. Cairns, J. Catafesta, C. Levelut, et al., "Giant Negative Linear Compressibility in Zinc Dicyanoaurate," *Nature Materials* 12 (2013): 212–216, https://doi.org/10.1038/nmat3551.

3. R. H. Baughman, S. Stafstrom, C. X. Cui, and S. O. Dantas, "Materials With Negative Compressibilities in One or More Dimensions," *Science* 279 (1998): 1522–1524, https://doi.org/10.1126/science.279.5356.1522.

4. A. B. Cairns and A. L. Goodwin, "Negative Linear Compressibility," *Physical Chemistry Chemical Physics* 17 (2015): 20449–20465, https://doi.org/10.1039/C5CP00442J.

5. A. L. Goodwin, D. A. Keen, and M. G. Tucker, "Large Negative Linear Compressibility of $Ag_3[Co(CN)]_6$," *Proceedings National Academy of Science USA* 105 (2008): 18708–18713.

6. F. Colmenero, "Negative Linear Compressibility in Nanoporous Metal–Organic Frameworks Rationalized by the Empty Channel Structural Mechanism," *Physical Chemistry Chemical Physics* 23 (2021): 8508–8524, https://doi.org/10.1039/D1CP00214G.

7. C. H. Woodall, C. M. Beavers, J. Christensen, et al., "Hingeless Negative Linear Compression in the Mechanochromic Gold Complex [$(C_6F_5Au)_2$ (-1,4-diisocyanobenzene)]," *Angewandte Chemie International Edition* 52 (2013): 9691–9694.

8. D. Caprini, F. Battista, P. Zajdel, et al., "Bubbles Enable Volumetric Negative Compressibility in Metastable Elastocapillary Systems," *Nature Communications* 15 (2024): 5076, https://doi.org/10.1038/s41467-024-49136-w.

9. D. Q. Jiang, T. Wen, Y. Z. Guo, et al., "Reentrant Negative Linear Compressibility in MIL-53(Al) Over an Ultrawide Pressure Range," *Chemistry of Materials* 34 (2022): 2764–2770, https://doi.org/10.1021/acs.chemmater.1c04398.

10. W. Z. Cai and A. Katrusiak, "Giant Negative Linear Compression Positively Coupled to Massive Thermal Expansion in a Metal–Organic Framework," *Nature Communications* 5 (2014): 4337, https://doi.org/10.1038/ncomms5337.

11. Y. S. Yu, Q. X. Zeng, Y. P. Chen, L. Jiang, K. Wang, and B. Zou, "Extraordinarily Persistent Zero Linear Compressibility in Metal-Organic Framework MIL-122(In)," *ACS Materials Letters* 2 (2020): 519–523, https://doi.org/10.1021/acsmaterialslett.0c00090.

12. K. E. Evans and A. Alderson, "Auxetic Materials: Functional Materials and Structures From Lateral Thinking!," *Advanced Materi-*

als 12 (2000): 617–628, https://doi.org/10.1002/(SICI)1521-4095(200005)12:9⟨617::AID-ADMA617⟩3.0.CO;2-3.

13. Y. Zhao, C. Z. Fan, C. Y. Pei, et al., "Colossal Negative Linear Compressibility in Porous Organic Salts," *Journal of the American Chemical Society* 142 (2020): 3593–3599, https://doi.org/10.1021/jacs.9b13274.

14. Z. A. Dreger, A. I. Stash, Z. G. Yu, Y. S. Chen, and Y. C. Tao, "High-Pressure Structural Response of an Insensitive Energetic Crystal: Dihydroxylammonium 5,5′-Bistetrazole-1,1′-diolate (TKX-50)," *Journal of Physical Chemistry C* 121 (2017): 5761–5767, https://doi.org/10.1021/acs.jpcc.7b00867.

15. Y. Qiao, K. Wang, H. Yuan, K. Yang, and B. Zou, "Negative Linear Compressibility in Organic Mineral Ammonium Oxalate Monohydrate With Hydrogen Bonding Wine-Rack Motifs," *Journal of Physical Chemistry Letters* 6 (2015): 2755–2760, https://doi.org/10.1021/acs.jpclett.5b01129.

16. A. D. Fortes, E. Suard, and K. S. Knight, "Negative Linear Compressibility and Massive Anisotropic Thermal Expansion in Methanol Monohydrate," *Science* 331 (2011): 742–746, https://doi.org/10.1126/science.1198640.

17. F. Occelli, P. Loubeyre, and R. Letoullec, "Properties of Diamond Under Hydrostatic Pressures up to 140 GPa," *Nature Materials* 2 (2003): 151–154, https://doi.org/10.1038/nmat831.

18. H. Cynn, J. E. Klepeis, C. S. Yoo, and D. A. Young, "Osmium Has the Lowest Experimentally Determined Compressibility," *Physical Review Letter* 88 (2002): 135701, https://doi.org/10.1103/PhysRevLett.88.135701.

19. B. K. Godwal, J. Yan, S. M. Clark, and R. Jeanloz, "High-Pressure Behavior of Osmium: An Analog for Iron in Earth's Core," *Journal of Applied Physics* 111 (2012): 112608, https://doi.org/10.1063/1.4726203.

20. L. Dubrovinsky, N. Dubrovinskaia, E. Bykova, et al., "The Most Incompressible Metal Osmium at Static Pressures Above 750 Gigapascals," *Nature* 525 (2015): 226–229.

21. Q. X. Zeng, K. Wang, and Zou, "Near Zero Area Compressibility in a Perovskite-Like Metal-Organic Frameworks $[C(NH_2)_3][Cd(HCOO)_3]$," *ACS Applied Materials & Interfaces* 10 (2018): 23481–23484.

22. X. X. Jiang, Y. Yang, M. S. Molokeev, et al., "Zero Linear Compressibility in Nondense Borates With a "Lu-Ban Stool"-Like Structure," *Advanced Materials* 30 (2018): 1801313, https://doi.org/10.1002/adma.201801313.

23. X. X. Jiang, M. S. Molokeev, L. Y. Dong, et al., "Anomalous Mechanical Materials Squeezing Three-Dimensional Volume Compressibility into One Dimension," *Nature Communications* 11 (2020): 5593, https://doi.org/10.1038/s41467-020-19219-5.

24. X. Jiang, S. Luo, L. Kang, et al., "Isotropic Negative Area Compressibility Over Large Pressure Range in Potassium Beryllium Fluoroborate and Its Potential Applications in Deep Ultraviolet Region," *Advanced Materials* 27 (2015): 4851–4857, https://doi.org/10.1002/adma.201502212.

25. D. Jiang, T. Wen, H. Song, et al., "Intrinsic Zero-Linear and Zero-Area Compressibilities Over an Ultrawide Pressure Range Within a *Gear-Spring* Structure," *CCS Chemistry* 4 (2022): 3246–3253, https://doi.org/10.31635/ccschem.022.202101739.

26. X. Y. Zhang, Y. Q. Liu, M. S. Molokeev, B. H. Xu, X. X. Jiang, and Z. S. Lin, "Realizing Persistent Zero Area Compressibility Over a Wide Pressure Range in Cu_2 GeO_4 by Microscopic Orthogonal-Braiding Strategy," *Angewandte Chemie International Edition* 63 (2024): e202318401, https://doi.org/10.1002/ange.202318401.

27. Q. Lai, Y. Y. Long, P. Yin, J. M. Shreeve, and S. P. Pang, "Thinking Outside the Energetic Box: Stabilizing and Greening High-Energy Materials With Reticular Chemistry," *Accounts of Chemical Research* 57 (2024): 2790–2803, https://doi.org/10.1021/acs.accounts.4c00330.

28. Y. Q. Qin, F. Yang, S. J. Jiang, M. Lu, and P. C. Wang, "A New Breakthrough in Electrochemical Synthesis of Energetic Materials: Constructing Super Heat-Resistant Explosives," *Chemical Engineering Journal* 486 (2024): 149968, https://doi.org/10.1016/j.cej.2024.149968.

29. Q. H. Zhang and J. M. Shreeve, "Energetic Ionic Liquids as Explosives and Propellant Fuels: A New Journey of Ionic Liquid Chemistry," *Chemical Reviews* 114 (2014): 10527–10574, https://doi.org/10.1021/cr500364t.

30. B. Dumas, O. Jobin, W. Kaprolat, J. Zahlawi, and E. Robert, "Ignition Delay and Performance of Sorbitol Based Hypergolic Hybrid Fuels," *Fuel* 349 (2023): 128417, https://doi.org/10.1016/j.fuel.2023.128417.

31. M. Born, J. Plank, and T. M. Klapötke, "Energetic Polymers: A Chance for Lightweight Reactive Structure Materials?," *Propellants, Explosives, Pyrotechnics* 47 (2022): e202100368, https://doi.org/10.1002/prep.202100368.

32. M. Tortora, P. Zajdel, A. R. Lowe, et al., "Giant Negative Compressibility by Liquid Intrusion into Superhydrophobic Flexible Nanoporous Frameworks," *Nano Letters* 21 (2021): 2848–2853, https://doi.org/10.1021/acs.nanolett.0c04941.

33. Q. L. Yan, F. Q. Z. Gozin, A. Cohen, and S. P. Pang, "Highly Energetic Compositions Based on Functionalized Carbon Nanomaterials," *Nanoscale* 8 (2016): 4799–4851, https://doi.org/10.1039/C5NR07855E.

34. C. C. Li, J. Tang, G. B. Cheng, C. Xiao, and H. W. Yang, "An Advanced Green Fused Diazonium Initiating Substance," *Journal of Materials Chemistry A* 12 (2024): 16367–16372, https://doi.org/10.1039/D4TA03236E.

35. Q. L. Yan and L. T. DeLuca, "Urgent Demand for High Energy Insensitive Propellants With Controllable Burn Rates," *Energetic Materials Frontiers* 2 (2021): 1–2, https://doi.org/10.1016/j.enmf.2021.03.004.

36. G. R. Lei, W. C. Cheng, Z. J. Lu, T. L. Zhang, Z. M. Li, and J. G. Zhang, "A Three-Dimensional Energetic Coordination Compound (BLG-1) With Excellent Initiating Ability for Lead-Free Primary Explosives," *Materials Horizons* 10 (2023): 5775–5781, https://doi.org/10.1039/D3MH01410J.

37. T. R. Ravindran, R. Rajan, and V. Venkatesan, "Review of Phase Transformations in Energetic Materials as a Function of Pressure and Temperature," *Journal of Physical Chemistry C* 123 (2019): 29067–29085, https://doi.org/10.1021/acs.jpcc.9b04885.

38. G. Y. Qi, Y. Cao, T. Y. Jiang, H. Zhang, and Y. Wang, "Structural Evolvement of 1-Methyl-3,4,5-Trinitropyrazole at High Pressure," *Energetic Materials Frontiers* 5 (2024): 90–95, https://doi.org/10.1016/j.enmf.2024.03.003.

39. G. Y. Qi, S. W. Song, Z. Y. Deng, et al., "Pressure-Induced Topochemical Polymerization Toward Advanced Energetic Materials," *CCS Chemistry* 5 (2023): 1815–1826, https://doi.org/10.31635/ccschem.022.202202249.

40. S. Aldridge, A. J. Downs, C. Y. Tang, et al., "Structures and Aggregation of the Methylamine−Borane Molecules, $Me_nH_{3-n}N{\cdot}BH_3$ (n = 1−3), Studied by X-ray Diffraction, Gas-Phase Electron Diffraction, and Quantum Chemical Calculations," *Journal of the American Chemical Society* 131 (2009): 2231–2243, https://doi.org/10.1021/ja807545p.

41. G. Belanger-Chabot, M. Rahm, R. Haiges, and K. O. Christe, "Ammonia-(Dinitramido) boranes: High-Energy-Density Materials," *Angewandte Chemie International Edition* 54 (2015): 11730–11734.

42. G. Y. Qi, K. Wang, G. J. Xiao, and B. Zou, "High Pressure, a Protocol to Identify the Weak Dihydrogen Bonds: Experimental Evidence of C–H···H–B Interaction," *Science China Chemistry* 61 (2018): 276–280, https://doi.org/10.1007/s11426-017-9152-8.

43. H. M. Rietveld, "The Rietveld method," *Physica Scripta* 89 (2014): 098002, https://doi.org/10.1088/0031-8949/89/9/098002.

44. J. Zhao, D. D. L. Wang, Z. Liu, et al., "Structure Stability and Compressibility of Iron-Based Superconductor $Nd(O_{0.88}F_{0.12})FeAs$ under High Pressure," *Journal of the American Chemical Society* 130 (2008): 13828–13829, https://doi.org/10.1021/ja804229k.

45. K. A. Irshad, P. Anees, R. Rajitha, et al., "Anomalous Lattice Compression in the Hexagonal La_2O_3 – A High Pressure X-ray Diffraction, Raman Spectroscopy and First Principle Study," *Journal of Alloys and Compounds* 822 (2020): 153657, https://doi.org/10.1016/j.jallcom.2020.153657.

46. M. J. Cliffe and A. L. Goodwin, "*PASCal*: A Principal Axis Strain Calculator for Thermal Expansion and Compressibility Determination,"

Journal of Applied Crystallography 45 (2012): 1321–1329, https://doi.org/10.1107/S0021889812043026.

47. H. Qiu, R. An, C. Cui, et al., "Bridging the Interlayer Binding to Ordered π-Conjugated Units for Constructing High-Performing Light Polarization Crystals," *Angewandte Chemie International Edition* 64 (2025): e202507171.

48. R. F. Guan, J. Y. Liu, A. Kutty, et al., "Pressure Mediated Phase Transition and Dihydrogen Bonding Formation in Trimethylamine Borane," *Journal of Materials Chemistry C* 12 (2024): 14833–14843, https://doi.org/10.1039/D4TC02285H.

49. D. Paliwoda, K. Kowalska, M. Hanfland, and A. Katrusiak, "U-Turn Compression to a New Isostructural Ferrocene Phase," *Journal of Physical Chemistry Letters* 4 (2013): 4032–4037, https://doi.org/10.1021/jz402254b.

50. M. Maczka, S. Sobczak, P. Ratajczyk, et al., "Pressure-Driven Phase Transition in Two-Dimensional Perovskite MHy_2PbBr_4," *Chemistry of Materials* 34 (2022): 7867–7877.

Supporting Information

Additional supporting information can be found online in the Supporting Information section.

Supporting File 1: Supporting information is available comprising fingerprint plots of TMAB at ambient pressure, high-pressure XRD measurement of TMAB, the linear compressibility of TMAB, high-pressure Raman, IR and absorption spectra of TMAB, Hirshfeld surface of TMAB at 10 and 20 GPa, the repeated in situ high-pressure Raman spectra of TMAB and experimental details (sample preparation and high-pressure generation including Figures S24–S26 and Table S4, S5, high-pressure measurement and computational methods). The authors have cited additional references within the Supporting information [46, 51–53].